Journal of ELECTRONIC MATERIALS, Vol. 48, No. 7, 2019
https://doi.org/10.1007/s11664-019-07211-9

Effect of Thermal Cycling on Interfacial Microstructure and Mechanical Properties of Sn-0.3Ag-0.7Cu-(α-Al_2O_3) Nanoparticles/Cu Low-Ag Solder Joints

JIE WU,[1,2] SONGBAI XUE,[1,4] JINGWEN WANG,[1] and PENG XUE[3]

1.—College of Materials Science and Technology, Nanjing University of Aeronautics and Astronautics, Nanjing 210016, People's Republic of China. 2.—Department of Mechanical, Aerospace and Biomedical Engineering, University of Tennessee Knoxville, 1512 Middle Drive, Knoxville, TN 37996, USA. 3.—School of Materials Science and Engineering, Nanjing University of Science and Technology, Nanjing 210094, China. 4.—e-mail: xuesb@nuaa.edu.cn

The evolution of interfacial microstructures and mechanical properties of joints soldered with Sn-0.3Ag-0.7Cu (SAC0307) and SAC0307-0.12Al_2O_3 nanoparticles (NPs) subjected to thermal cycling were investigated. The joint soldered with SAC0307-0.12Al_2O_3 displayed an enhanced thermal cycling shear force with a ductile fracture mode when compared with the original alloy whose fracture mode showed a mixed feature of ductile and brittle. The enhanced thermal cycling shear force was attributed to a pinning effect by Al_2O_3 NPs on interfacial IMC grain growth. Even after 1200 thermal cycles, SAC0307-0.12Al_2O_3 solder was still structurally characterized by a much more refined microstructure than the non-reinforced solder alloy. Theoretical analysis on the growth of interfacial IMC layer showed that with the addition of Al_2O_3 NPs, the average growth coefficients of total interfacial IMCs (D_T) and Cu_3Sn IMCs (D_{Cu_3}) were decreased from 9.2×10^{-11} cm^2/h to 5.6×10^{-11} cm^2/h, and from 6.9×10^{-11} cm^2/h to 4.1×10^{-11} cm^2/h, respectively. Hence, a much thinner IMC layer was produced at the SAC0307-0.12Al_2O_3/Cu interface, thus contributing to an enhanced shear resistance.

Key words: Al_2O_3 nanoparticles, thermal cycling, interfacial microstructure, shear force

INTRODUCTION

The joining of electronic devices and conductive substrates has been increasingly studied to due to its important role in mechanical, electrical and thermal supports.[1,2] Therefore, improving the joint strength becomes particularly critical to ensure the normal working of joints in harsh environments, such as a repeat turn on and off, long-term operation, sweat corrosion, and so on.[3–5] From the view of microstructural properties, the mechanical performance of a single solder joint usually depends on the interfacial intermetallic compounds (IMCs) formed at the solder/substrate interface.[6,7] It is well established that solder with a refined microstructure combined with a thin, flat interfacial IMC layer formed at the solder joint generally results in good mechanical properties.[8,9] To achieve this, various methods of alloying[10–12] and depositing barrier metallic films (e.g., Au[13,14] and Ni[15,16]) are widely accepted. Among them, alloying has been emphasized more due to its capacity to modify other properties of Sn-based solders.[17] Despite the variety of foreign alloys, the most appropriate alloys are generally those with surface-active characteristics like Ga or rare earth elements.[18–20] This is because these surface-active alloys can be spontaneously adsorbed on the grain surfaces of β-Sn phases or related IMCs to pin their growth. Currently, with the development of nano-scaled materials,

(Received October 25, 2018; accepted April 9, 2019; published online May 2, 2019)

researchers have also begun to select them as reinforced materials due to their unique properties of high surface free energy and large specific surface area.[21–27] It has been demonstrated that, when reinforcing solder with NPs, a higher mechanical property can be attained. Sun et al.[28] doped Al NPs into Sn-1.0Ag-0.5Cu solder and found that the joint soldered with Sn-Ag-Cu-0.1Al NPs had higher thermal cycling (TC) shear force than that soldered with Sn-Ag-Cu. Although lead-free solder reinforced with NPs has been widely fabricated in recent years, their TC mechanical properties have rarely been studied.

So far, Sn-Ag-Cu solder has been commonly used as a reinforced target mainly because of its relatively better comprehensive properties compared with other substitutes for Sn-Pb solder, such as Sn-Cu, Sn-Ag, and Sn-Zn solders.[29,30] In general, the high Ag content in Sn-Ag-Cu solder leads to high production costs and easy formation of plate-like Ag_3Sn IMCs,[31] thus causing a degradation of drop reliability. Unfortunately, reducing the Ag content in Sn-Ag-Cu solder also triggers some other issues, such as excessive growth of interfacial Cu_6Sn_5 IMCs, directly degrading the joint strength.[32,33] To offset the issues caused by reducing the Ag content, in our previous study we doped Al_2O_3 NPs with varying contents into Sn-0.3Ag-0.7Cu low-Ag solder,[34] and the results showed a positive effect of doping 0.12 wt% Al_2O_3 NPs on an inhibiting interfacial IMC layer growth and a resultant enhanced shear force of the solder joint. Our previous work put emphasis on the inhibiting effect of Al_2O_3 NPs on the growth of interfacial IMCs in solid–liquid reactions, while their influence on the solid–solid reaction has not been studied, and the underlying mechanism remains enigmatic.

Hence, in this work, the evolution of the interfacial microstructure of Sn-0.3Ag-0.7Cu (SAC0307)/Cu and SAC0307-0.12Al_2O_3/Cu solders subjected to different thermal cycles was investigated. Based on the experimental results, the influence of Al_2O_3 NPs on the growth kinetics of interfacial IMCs at the solder/Cu interface in the solid-state reaction process has been discussed. In addition, the shear forces of two types of solder joints subjected to various thermal cycling has been evaluated by shear testing and the corresponding fracture morphology has also been given to better understand the microstructure–property relationship.

EXPERIMENTAL

SAC0307-0.12Al_2O_3 low-Ag composite solder was prepared by mechanically blending 0.12 wt% Al_2O_3 nanoparticles (~ 50 nm) into SAC0307 solder paste, as detailed in our previous study .[34] Afterwards, to observe the microstructure evolution at the solder/Cu interface subjected to thermal cycling treatment, interfacial samples were made through soldering these two kinds of solders on Cu substrates in a reflow furnace. The T_{max} of the reflow process was set as ~ 245°C and the whole reflow time from the heating stage to the cooling stage was about 475 s. The detailed reflow profile can be found in our previous paper.[34] Figure 1 shows the corresponding thermal cycling curve: the highest and lowest temperatures of the thermal cycle are 125°C and − 55°C, respectively., and the dwell-time is 20 min. Both the ascendant rate and the descendant rate are 18°C/min. The entire process of thermal cycling lasts for 1200 cycles and the sample observation is conducted after each 200 thermal cycles. Before the morphology observation, interfacial samples were polished and corroded with 5% HNO_3-alcohol solution. Consequently, sample observation and analysis were conducted with the aid of scanning electron microscopy (SEM) equipped with energy dispersion spectrum (EDS) and a backscattered electron (BSE) detector. The thickness of the interfacial IMC layer was measured by Image Pro-plus software.[35,36]

To discover the effect of thermal cycling on the shear forces of the joints soldered with the two kinds of solders, joint samples were also subjected to the aforementioned thermal cycling environment. The joint samples were obtained by soldering 0805 ceramic resistors on a printed circuit board (Cu/Ni/Au pad) using the studied solders. Afterwards, a push-type broach equipped in the STR-1000 Microjoint strength tester (Rhesca, Japan; Fig. 2) was added to test their shear forces after thermal cycling. The shearing speed was set as 10 mm/min and the shear tool stand-off height was 20 μm when the shearing process began, and was the same for all the samples. Each test was undertaken five times and the average value served as the final result. After the shearing tests, the morphology of the fractured joint was observed by SEM and analyzed by EDS.

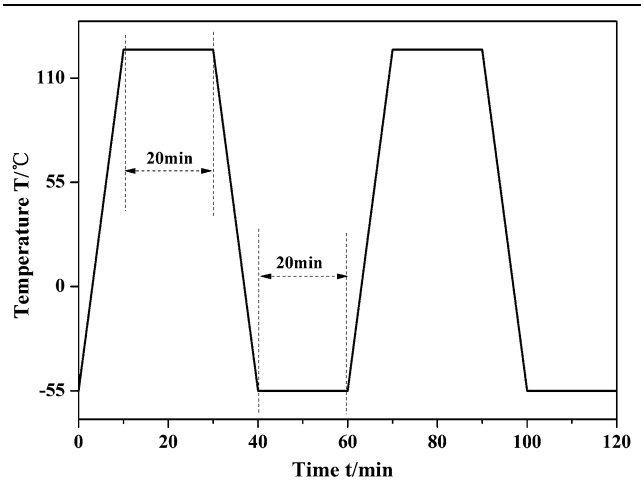

Fig. 1. Loading temperature cycle curve.

RESULTS AND DISCUSSION

Evolution of Interfacial Microstructure

Figure 3 shows the cross-sectional images of interfacial microstructures of SAC0307/Cu solder joints subjected to thermal cycling. It is clear that, after 200 thermal cycles, Ag_3Sn particles in the solder matrix still remained at nano-scale (Fig. 3a), while Cu_6Sn_5 IMCs showed a little coarsening. After 400 thermal cycles, the coarsening of Cu_6Sn_5 continued, along with a slight growth of Ag_3Sn IMCs (Fig. 3b). With the increment in the thermal cycles to 1200, the sizes of the Cu_6Sn_5 IMCs became larger (Fig. 3c–f) and Ag_3Sn IMCs further grew to a micro-scale (Fig. 3f). The morphology evolution of SAC0307-0.12Al_2O_3/Cu solder joints subjected to the identical thermal cycling is also shown in Fig. 4. Similarly, with the increased number of thermal cycles, IMCs of Cu_6Sn_5 and Ag_3Sn also gradually coarsened, but with a much lower growth rate than those in the SAC0307/Cu joint matrix (Fig. 3a–f). This is attributed to the adsorption of Al_2O_3 NPs on the grain surfaces of the IMCs, having a pinning effect on their growth. Hence, the atom diffusion will be evidently hindered even in the high-temperature stage of thermal cycling. Consequently, related IMCs can keep a relatively refined state and play a mechanical strengthening role in the solder. Moreover, the total thickness of the interfacial IMCs layer at both interfaces of SAC0307/Cu and SAC0307-0.12Al_2O_3/Cu increased with the thermal cycles, along with forming a new IMCs layer with darker contrast at the bottom of the Cu_6Sn_5 IMC layer, whose morphology evolution will be described in detail in the next section.

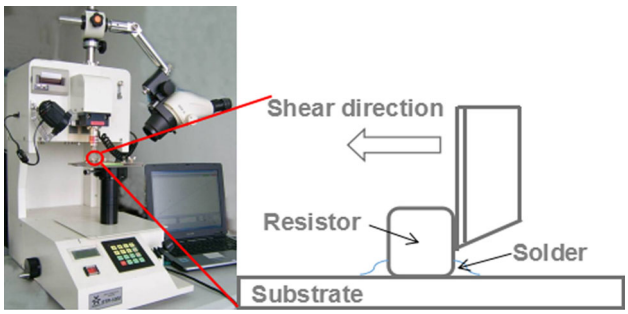

Fig. 2. Sketch of shear test.

Evolution of Interfacial IMC Layer

Figures 5 and 6 show the BSE micrographs of interfacial IMC layers forming at the interfaces of SAC0307/Cu and SAC0307-0.12Al_2O_3/Cu, respectively. After an initial 200 thermal cycles, a continuous hill-like interfacial Cu_6Sn_5 IMC layer was observed at the SAC0307/Cu interface (Fig. 5a). With an increment in the number of thermal cycles, the thickness of the interfacial Cu_6Sn_5 IMC layer increased, along with gradually increased radii (Fig. 5b–f). In particular, a new interfacial IMC layer with dark contrast, identified as Cu_3Sn via EDS analysis (Fig. 5f), also formed at the bottom of the interfacial Cu_6Sn_5 IMC layer, and its thickness increased with the number of thermal cycles. Unlike the interfacial IMC layer at the SAC0307/Cu interface, that which developed at the SAC0307-

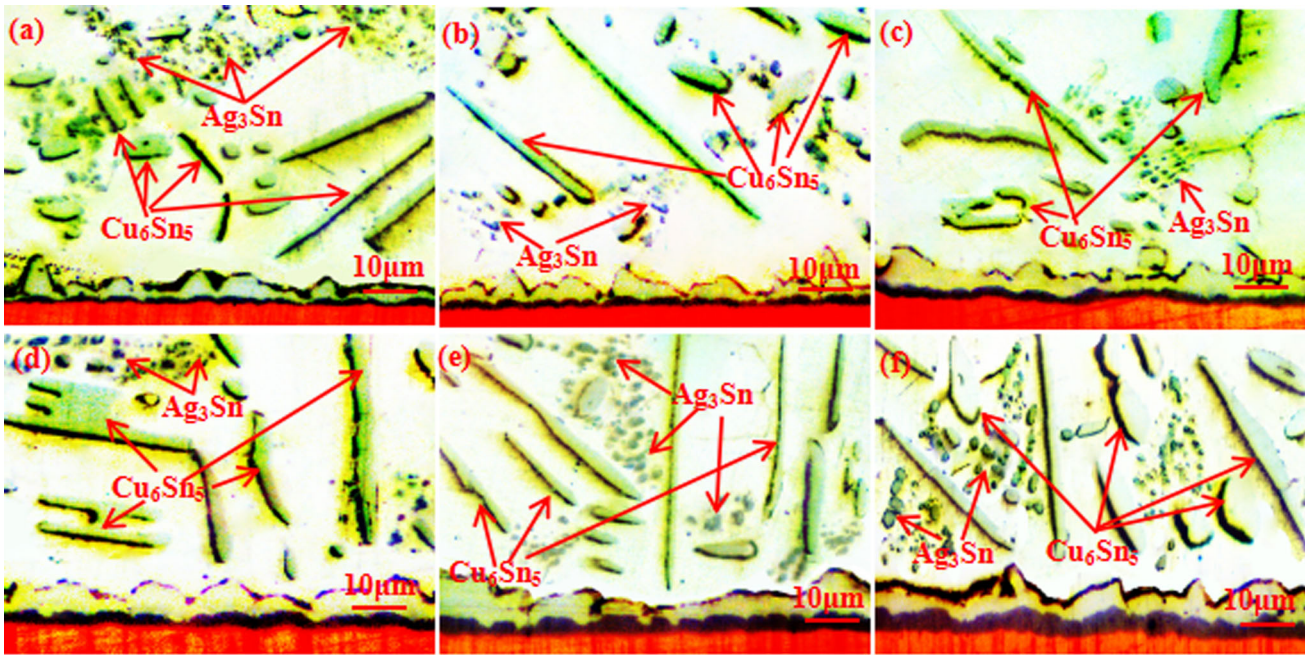

Fig. 3. Cross-sectional images of the microstructure at SAC0307/Cu interfaces subjected to thermal cycling: (a) 200 cycles; (b) 400 cycles; (c) 600 cycles; (d) 800 cycles; (e) 1000 cycles; (f) 1200 cycles.

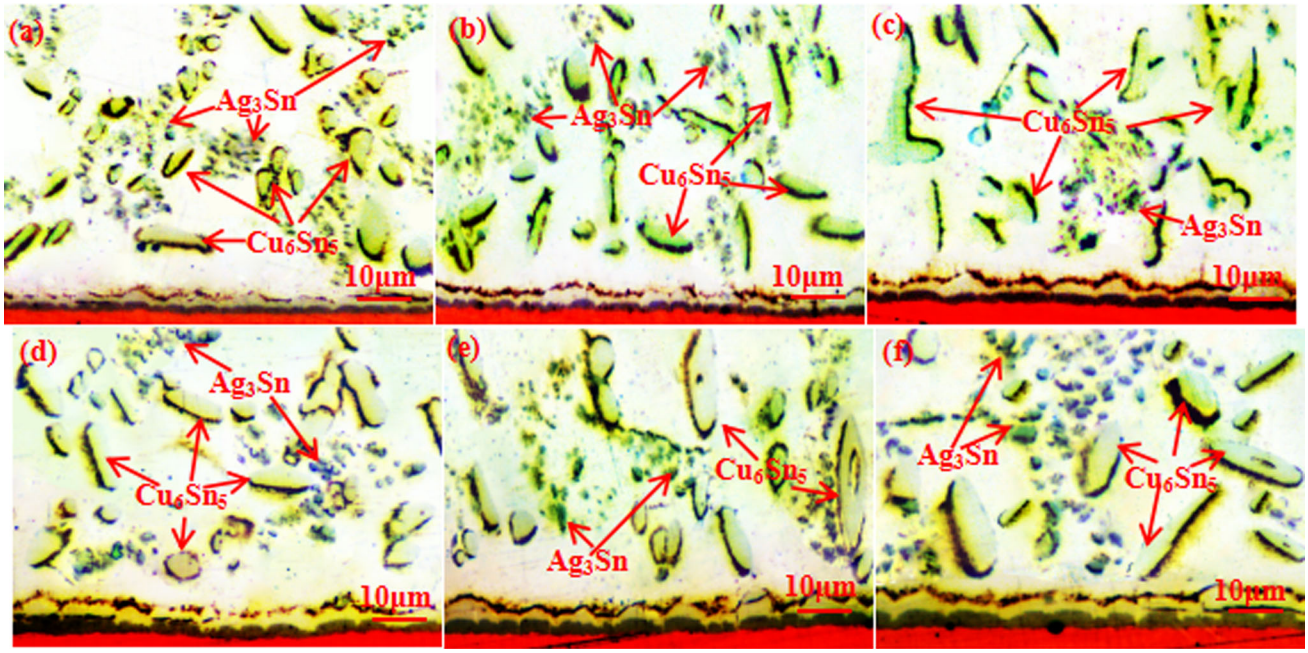

Fig. 4. Cross-sectional images of microstructure at SAC0307-0.12 Al_2O_3/Cu interfaces subjected to thermal cycling: (a) 200 cycles; (b) 400 cycles; (c) 600 cycles; (d) 800 cycles; (e) 1000 cycles; (f) 1200 cycles.

0.12Al_2O_3/Cu interface exhibited a much flatter morphology without any sharp protrusions (Fig. 6a–f). This is attributed to the surface-active characteristic of Al_2O_3 NPs, which allows them to be adsorbed on the grain surfaces of interfacial Cu_6Sn_5 IMCs, thereby pinning their growth. In this case, each interfacial Cu_6Sn_5 IMC had a similar, low-growth speed, and consequently a flat interfacial IMC layer was formed. Also, compared with the Cu_3Sn IMC layer formed at the SAC0307/Cu interface, a thinner layer with dark contrast was also observed to emerge at the bottom of the interfacial Cu_6Sn_5 IMC layer at the SAC0307-0.12Al_2O_3/Cu interface, with increased thickness with extending thermal cycles. Especially, with the thermal cycles increased to 1200, a few black particles emerged near the interface of SAC0307-0.12Al_2O_3/Cu (Fig. 6f). After EDS analysis on area B in Fig. 6f, these black particles were preliminarily identified as Al_2O_3 particles according to the Al/O atom ratio (Fig. 6g). To make a further confirmation, EDS mapping analysis was also undertaken, as displayed in Fig. 7a–f. It can be observed that the EDS mappings of Al and O (Fig. 7b, c) were bright in the location of the black particles, which confirms that those black particles are likely to be Al_2O_3 particles.

The average thicknesses of the total interfacial Cu_6Sn_5 and Cu_3Sn IMC layers as well as the separate Cu_3Sn IMC layer of these two types of solder joints subjected to different numbers of thermal cycles are summarized in Table I. Clearly, both solder joints observed an increase in the average thickness of the IMC layer, while the one growing at the SAC0307-0.12Al_2O_3/Cu interface had a much lower growth rate. After 1200 thermal cycles, the thickness of the interfacial IMC layer at the SAC0307/Cu interface grew to $\sim 8.2\ \mu$m, while that at the SAC0307-0.12Al_2O_3/Cu interface only reached $\sim 5.1\ \mu$m. It is well known that the growth of the interfacial IMC layer is mainly related to the diffusion during thermal cycles. In this research, considering different temperatures in one cycle, the conception of an average diffusion coefficient ($\bar{D}$) can be defined. As is well known, the thickness of the IMC layer at the solid diffusion interface satisfies the following classic diffusion formula:

$$x_t = x_0 + \sqrt{\bar{D}t}, \tag{1}$$

where x_t is the thickness of the interfacial IMC after a certain growth time t, x_0 is the initial thickness, D is the diffusion coefficient, which can be obtained from the slope of the linear-fitted curve, for the thickness of the interfacial IMC layer with growth time. Accordingly, a relationship between the thickness of the interfacial IMC layer (Cu_6Sn_5 + Cu_3Sn and Cu_3Sn) and the square root of the thermal cycling time (t_c) can be built, as shown in Fig. 8. Clearly, a nearly linear relationship between the IMC layer thickness and t_c was obtained, and the fitted equations are as follows:

$$x_t = x_0 + \sqrt{Dt} \tag{2}$$

where x_t is the thickness of the interfacial IMC after a certain growth time t, x_0 is the initial thickness, D is the diffusion coefficient, which can be obtained from the slope of the linear-fitted curve, for the

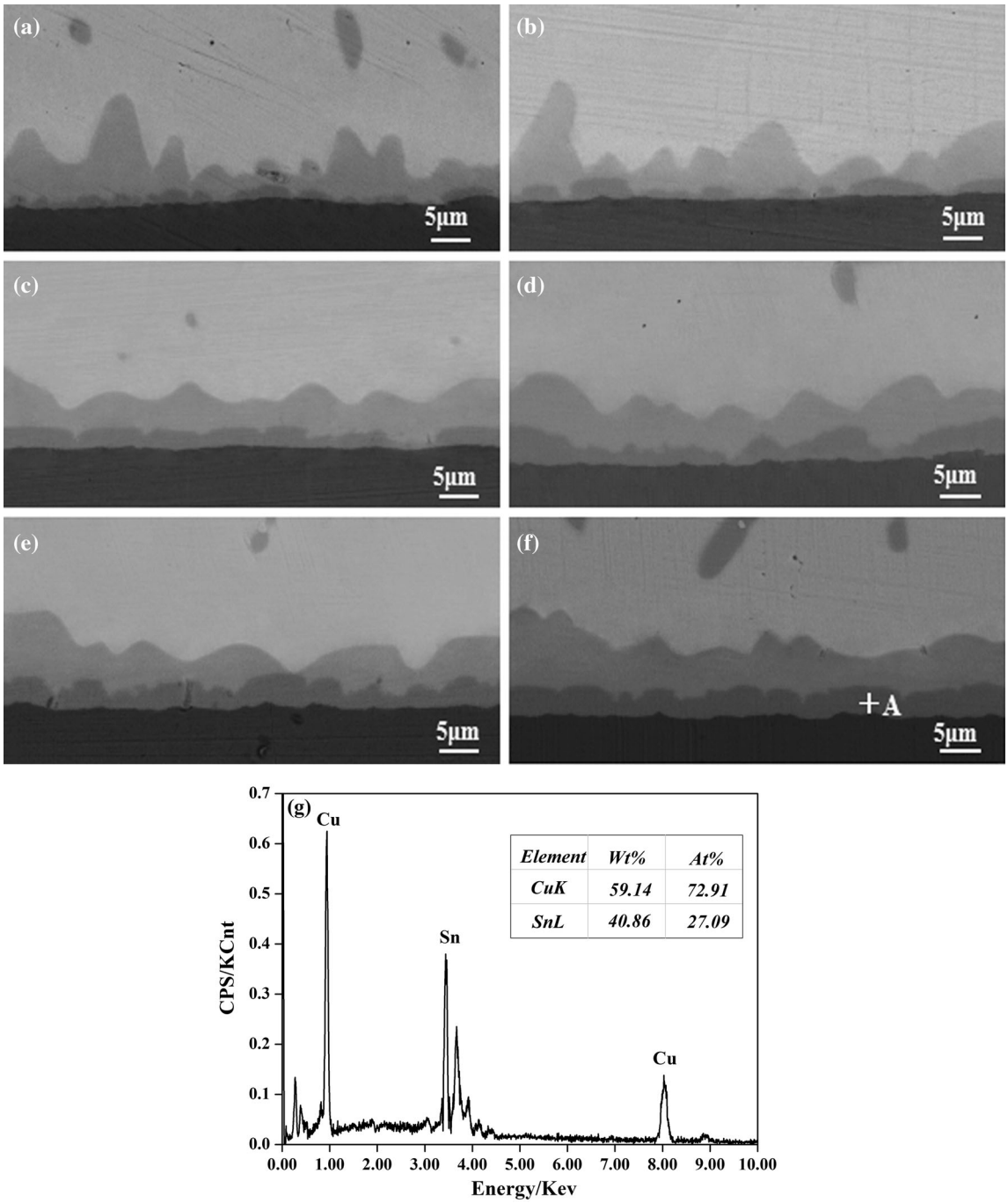

Fig. 5. BSE images of interfacial morphology at the SAC0307/Cu interface subjected to thermal cycling: (a) 200 cycles; (b) 400 cycles; (c) 600 cycles; (d) 800 cycles; (e) 1000 cycles; (f) 1200 cycles; (g) EDS analysis of Point A in (f).

interfacial IMC thickness with growth time. Accordingly, a relationship between IMC thickness (Cu_6Sn_5 + Cu_3Sn and Cu_3Sn) and the square root of thermal cycling time (t_c) can be built, as shown in Fig. 8. Clearly, a nearly linear relationship between IMC thickness and t_c was obtained and the fitted equations are as follows:

$$T_{(\mathrm{SAC0307-total})} = 4.7 + 0.096 \cdot \sqrt{t_c}; \quad T_{(\mathrm{SAC0307-Cu_3Sn})} = 0.083 \cdot \sqrt{t_c} \tag{3}$$

$$T_{(\mathrm{SAC0307-Al_2O_3-total})} = 2.6 + 0.075\sqrt{t_c}; \quad T_{(\mathrm{SAC0307-Al_2O_3-Cu_3Sn})} = 0.064\sqrt{t_c} \tag{4}$$

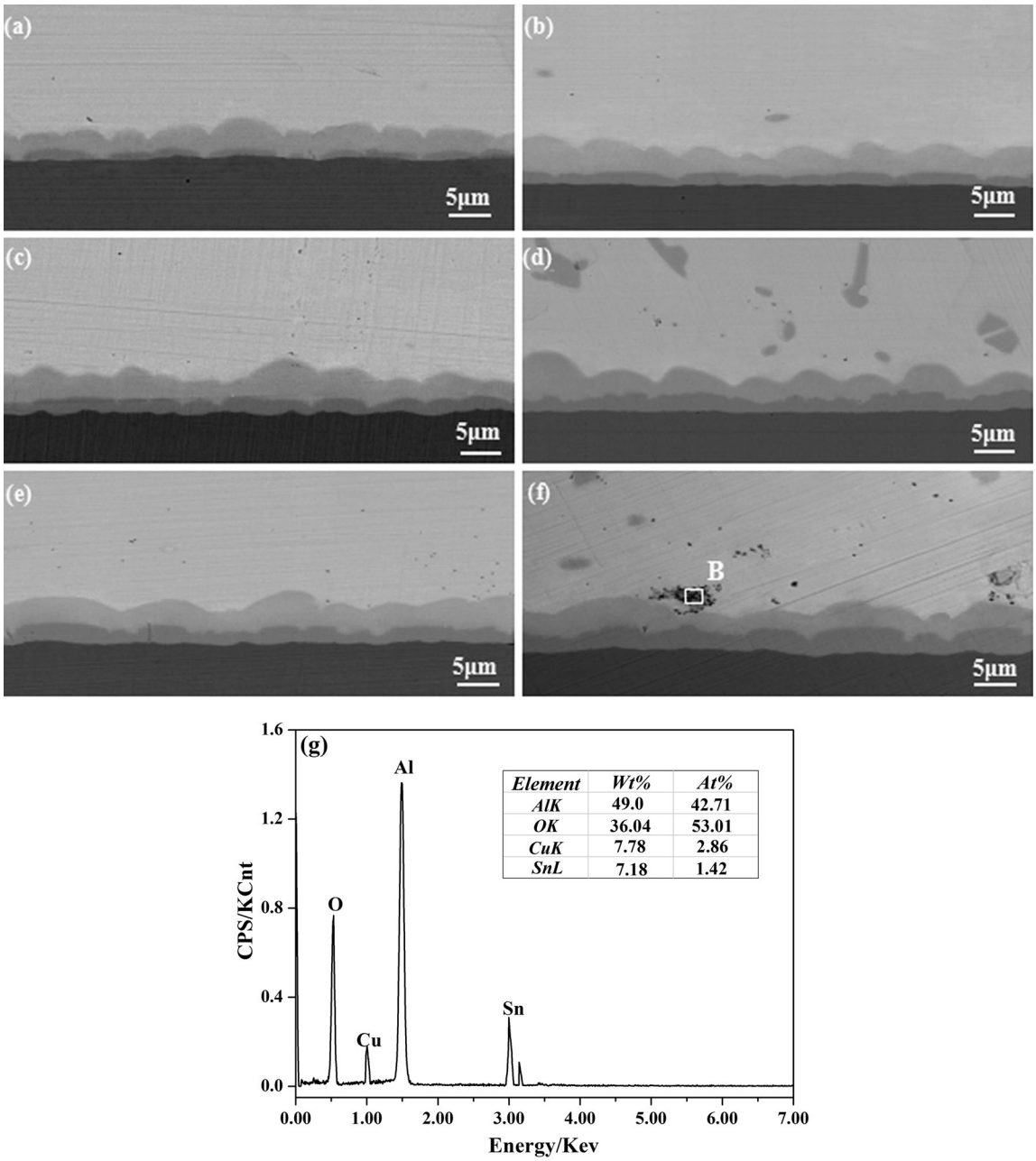

Fig. 6. BSE images of interfacial morphology at the SAC0307-0.12Al_2O_3/Cu interface subjected to thermal cycling: (a) 200 cycles; (b) 400 cycles; (c) 600 cycles; (d) 800 cycles; (e) 1000 cycles; (f) 1200 cycles; (g) EDS analysis of area B in (f).

It can be seen that doping 0.12 wt% Al_2O_3 NPs effectively decreased the average growth coefficients of both total interfacial IMCs ($\bar{D}_T$) and Cu_3Sn IMCs ($\bar{D}_{Cu_3}$), from 9.2×10^{-11} cm^2/h to 5.6×10^{-11} cm^2/h, and from 6.9×10^{-11} cm^2/h to 4.1×10^{-11} cm^2/h, respectively. This decrease in the values of $\bar{D}_T$ mainly benefited from the pinning effect of Al_2O_3 NPs on the growth of the interfacial Cu_3Sn IMC. However, the underlying mechanism for the growth inhibition of the interfacial Cu_3Sn IMC ($\bar{D}_{Cu_3}$) is mainly due to the decreased concentration gradient of Sn atoms at the Cu_6Sn_5/Cu_3Sn interface caused by the Al_2O_3 NPs as obstacles. Moreover, it was found that the growth constant of the Cu_3Sn IMC ($\bar{D}_{Cu_3}$) was a little larger than that of the interfacial Cu_6Sn_5 IMC ($\bar{D}_{Cu_6}$), which can be explained as follows. During the solder interface, the interfacial Cu_6Sn_5 IMC may be formed in two ways. One is to form directly

$$6Cu + 5Sn \rightarrow Cu_6Sn_5 \quad (5)$$

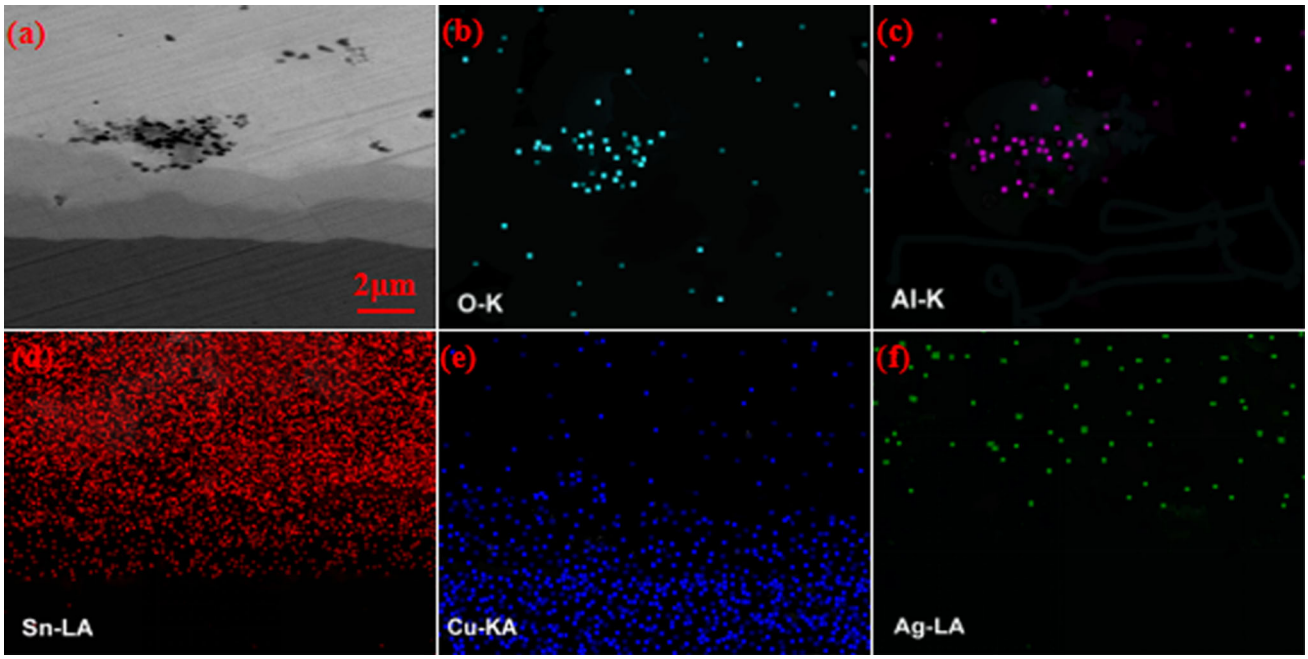

Fig. 7. (a) Magnified BSE images of the interfacial morphology at the SAC0307-0.12Al_2O_3/Cu interface subjected to 1200 thermal cycles; (b–f) EDX element mappings of the distribution of Sn, Ag, Cu, O, and Al, respectively.

Table I. Thickness of Cu_6Sn_5 and Cu_3Sn interfacial IMC layers

		Thermal cycles						
Solder	**Thickness (μm)**	**0**[34]	**200**	**400**	**600**	**1000**	**1200**	**1400**
SAC0307	Total (Cu_6Sn_5 + Cu_3Sn)	4.9	5.9	6.4	7.1	7.5	7.7	8.2
	Cu_3Sn	0	1.0	1.4	1.9	2.4	2.5	2.8
SAC0307-0.12Al_2O_3	Total (Cu_6Sn_5 + Cu_3Sn)	2.6	3.4	4.1	4.5	4.7	5.0	5.1
	Cu_3Sn	0	0.7	1.0	1.5	1.7	1.9	2.2

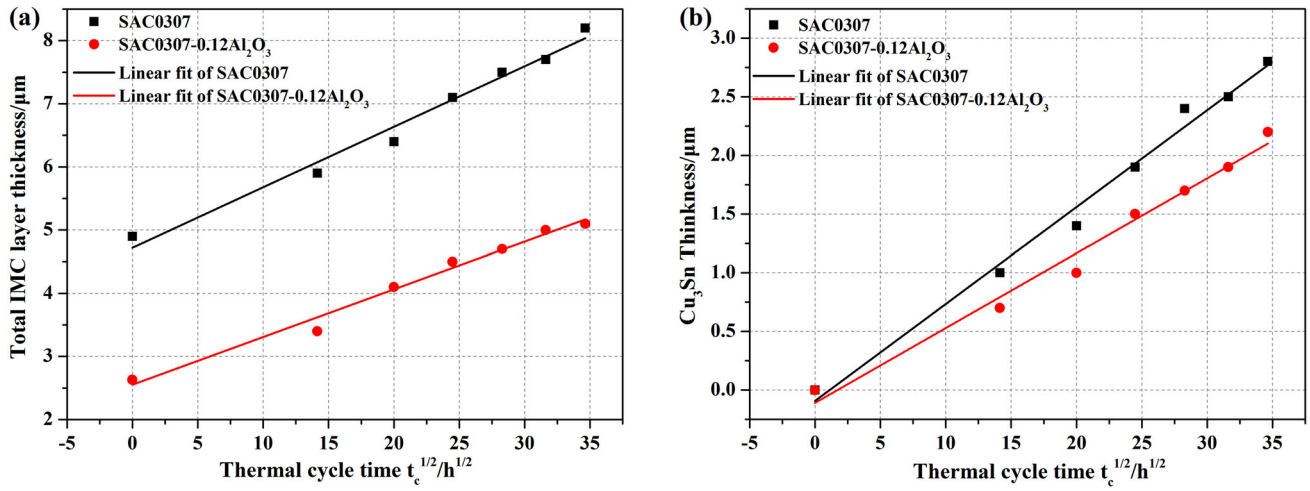

Fig. 8. Average thickness of the (a) total interfacial IMCs and (b) Cu_3Sn IMC at the interfaces of SAC0307/Cu and SAC0307-0.12Al_2O_3/Cu subjected to the thermal cycling.

and the other is to form by sacrificing the interfacial Cu_3Sn IMCs

$$2Cu_3Sn + 3Sn \rightarrow Cu_6Sn_5. \quad (6)$$

Similarly, there are also two possible approaches, including direct and indirect, for the growth and development of the interfacial Cu_3Sn IMC. The direct way is

$$3Cu + Sn \rightarrow Cu_3Sn, \quad (7)$$

while the indirect way is

$$Cu_6Sn_5 + 9Cu \rightarrow 5Cu_3Sn. \quad (8)$$

By comparison, it can be found that, when the interfacial Cu_6Sn_5 and Cu_3Sn IMCs form in direct ways (Eqs. 5, 7), per unit of Cu_6Sn_5 demands more Sn atoms than that of Cu_3Sn. When Cu_6Sn_5 and Cu_3Sn IMCs form in indirect ways (Eqs. 6, 8), the growth of Cu_6Sn_5 still requires a supply of Sn atoms, whereas that of Cu_3Sn demands abundant feeding of Cu atoms. Therefore, it can be concluded that the diffusion flux of Sn atoms dominates the development of Cu_6Sn_5, while that of Cu atoms and the interface state of Cu_3Sn/Cu_6Sn_5 mainly controls the growth of Cu_3Sn. Doping Al_2O_3 NPs into the solder matrix (the only Sn sources) can impede the diffusion of Sn atoms, thus effectively controlling the growth of the interfacial Cu_6Sn_5 IMC. However, in addition to the direct way that requires Sn atoms, the growth of Cu_3Sn IMC can also proceed by the indirect approach (Eq. 8). Thus, the growth constant of ($\bar{D}_{Cu_3}$) is a little larger than that of interfacial Cu_6Sn_5 IMCs ($\bar{D}_{Cu_6}$).

Shear Force and Fracture Morphology

After thermal cycling, shear tests were conducted on the two kinds of joints to evaluate their thermal cycling shear force. Figure 9 shows the change of shear forces of the solder joints with the number of thermal cycles. Clearly, with the number of thermal cycles increasing, the shear force of both joints first reduces slowly and then rapidly deteriorates. It should be noted that the SAC0307-0.12Al_2O_3/Cu solder joint exhibited a higher shear force than the SAC0307/Cu solder joint, irrespective of the number of thermal cycles. After 1200 thermal cycles, the shear force of the SAC0307/Cu and SAC0307-0.12Al_2O_3/Cu solder joints dropped to 19.8 N and 27.3 N, respectively. This enhancement in the thermal cycling shear force can be attributed to the improved joint microstructure, including solder matrix refinement and thinning of the interfacial IMC layer thickness, caused by doping 0.12 wt% Al_2O_3 NPs.

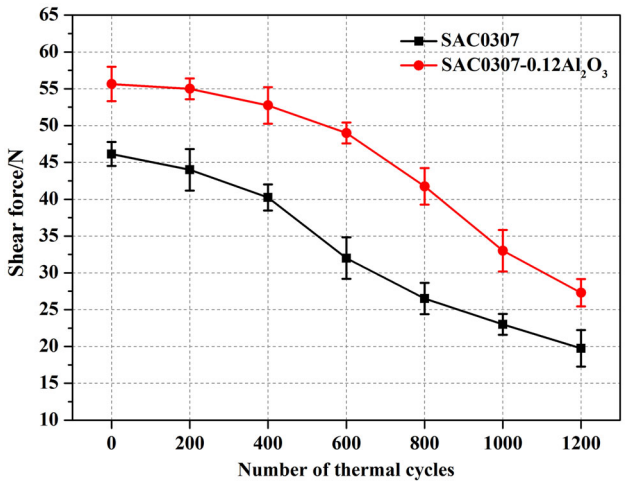

Fig. 9. Evolution of shear forces of SAC0307/Cu and SAC0307-0.12Al_2O_3/Cu solder joints subjected to thermal cycling.

In order to further understand the strengthening mechanism, the fracture surfaces of these two types of joints after thermal cycling were observed using SEM. Figures 10 and 11 show the fracture surfaces of the joints soldered with SAC0307 and SAC0307-0.12Al_2O_3, respectively. It is clear from Fig. 10a that, after 200 thermal cycles, elongated slant dimples parallel to shear loading direction were found on the fracture surface of the as-soldered SAC0307/Cu joint, indicating a mode of ductile fracture. The corresponding EDS analysis on area C (Fig. 10g) showed its main composition was pure Sn, which means that the fracture occurred from the solder matrix. With the number of thermal cycles increased from 200 to 800, despite the occurrence of ductile fractures in the SAC0307/Cu joints, slant dimples became larger and more superficial, as shown in Fig. 10a–d. These joints seemed to fracture from the solder matrix. This indicates that the shear strength of one solder joint is mainly dependent on the quality of the solder itself rather than the thickness of the interfacial IMCs, which is consistent with the results in Ref. 37. Worthy of note is that, as the number of thermal cycles increased to 1000 and then to 1200, the fracture surface became flatter and a relatively rough surface composed of many dark particles appeared (Fig. 10e, f). Based on the EDS analysis on area D, this region is identified as Cu_6Sn_5 according to its Cu/Sn ratio (Fig. 10h). Thus, it can be inferred that, with the number of thermal cycles increasing, the fracture location transferred from the bulk solder to the interface. This is mainly due to the growth of the interfacial IMC layer and the thermal expansion mismatch between the solder and the Cu_6Sn_5 which induced the formation of micro-cracks. Moreover, some river patterns besides large dimples also emerged on the fracture surface of the SAC0307/Cu solder joint after 1200 thermal cycles. Hence, it can be determined that the fracture mode of the joint soldered with SAC0307 changed from ductile to a mixed mode of ductile and brittle with increasing thermal cycles.

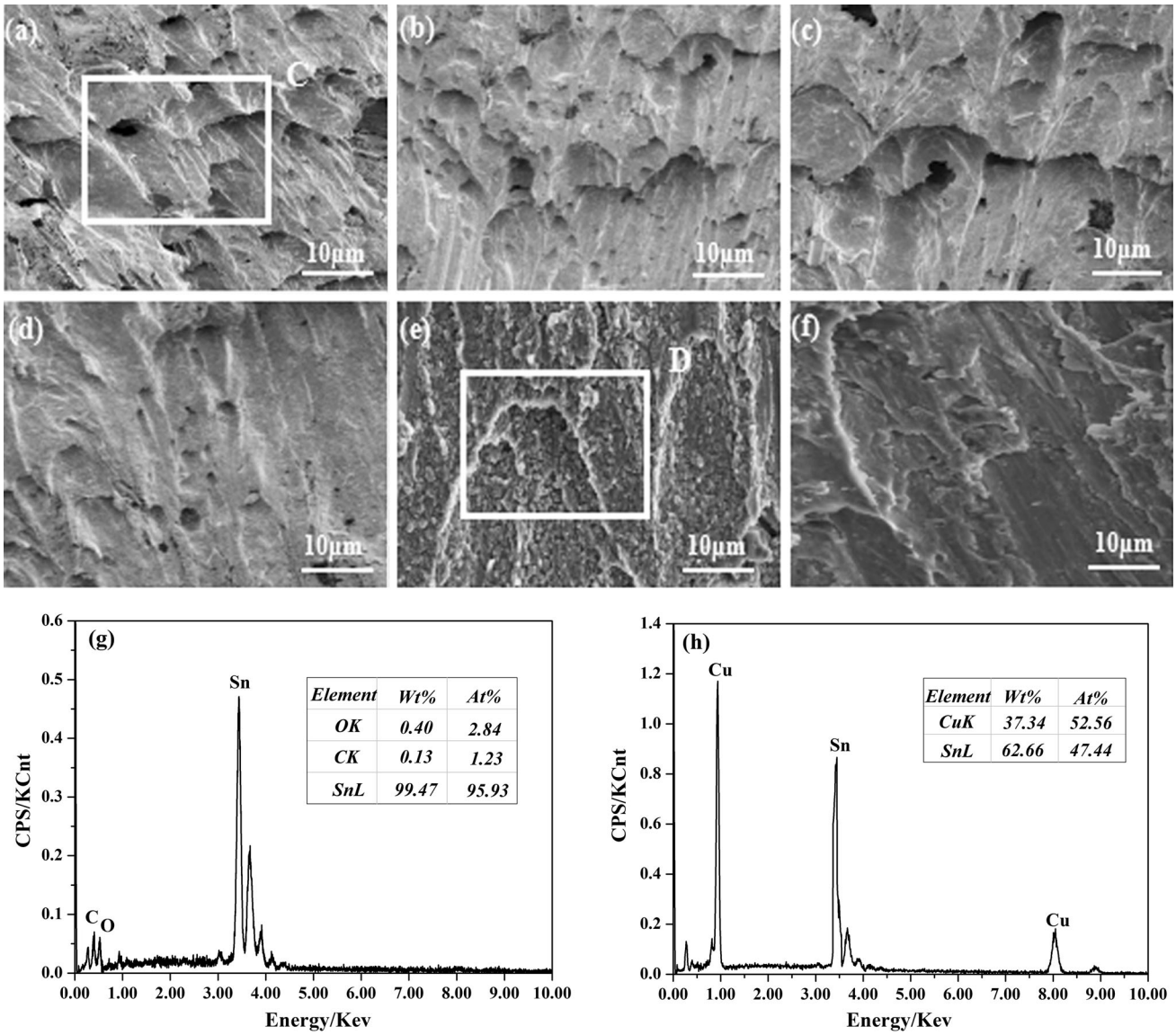

Fig. 10. Evolution of the fracture morphology of the SAC0307/Cu solder joint subjected to thermal cycling: (a) 200 cycles; (b) 400 cycles; (c) 600 cycles; (d) 800 cycles; (e) 1000 cycles; (f) 1200 cycles; (g) EDS analysis of area C in (a); (h) EDS analysis of area D in (e).

For the SAC0307-0.12Al_2O_3/Cu solder joints, a ductile fracture was observed after the initial 200 thermal cycles, but the dimples on the fracture surface were smaller than those on the fracture surface of the SAC0307/Cu joint (Fig. 11a). Also, compared with the dimples on the fracture surface of the SAC0307/Cu joint, those on the fracture surface of the SAC0307-0.12Al_2O_3/Cu joint were more rounded, indicative of an increased modulus of elasticity. With the increasing number of thermal cycles, the sizes of the dimples continued to increase but were still smaller than those on the fracture surface of the SAC0307/Cu joint (Fig. 11b–e). In addition, after 1200 thermal cycles, the newly formed IMCs were observed on the bottom of the dimples, identified as Cu_6Sn_5 IMCs by EDS analysis. In addition, some particles were also observed to lie on the bottom of the dimples, and confirmed as Al_2O_3 particles according to the EDS analysis on point G (Fig. 11g). These Al_2O_3 agglomerations were responsible for the accelerated fracture of the joint. Compared with the fracture behavior of the joint soldered with SAC0307, the fracture of the SAC0307-0.12Al_2O_3/Cu joint did not transfer to the interface even after 1200 thermal cycles. This also demonstrated the effective pinning effect of Al_2O_3 NPs on the growth of the interfacial IMC layer, contributing to the ductile fracture behavior with a higher shear force.

CONCLUSIONS

In this paper, the effect of Al_2O_3 NPs (0.12 wt%) on the evolution of interfacial microstructures and mechanical properties of joints soldered with Sn-

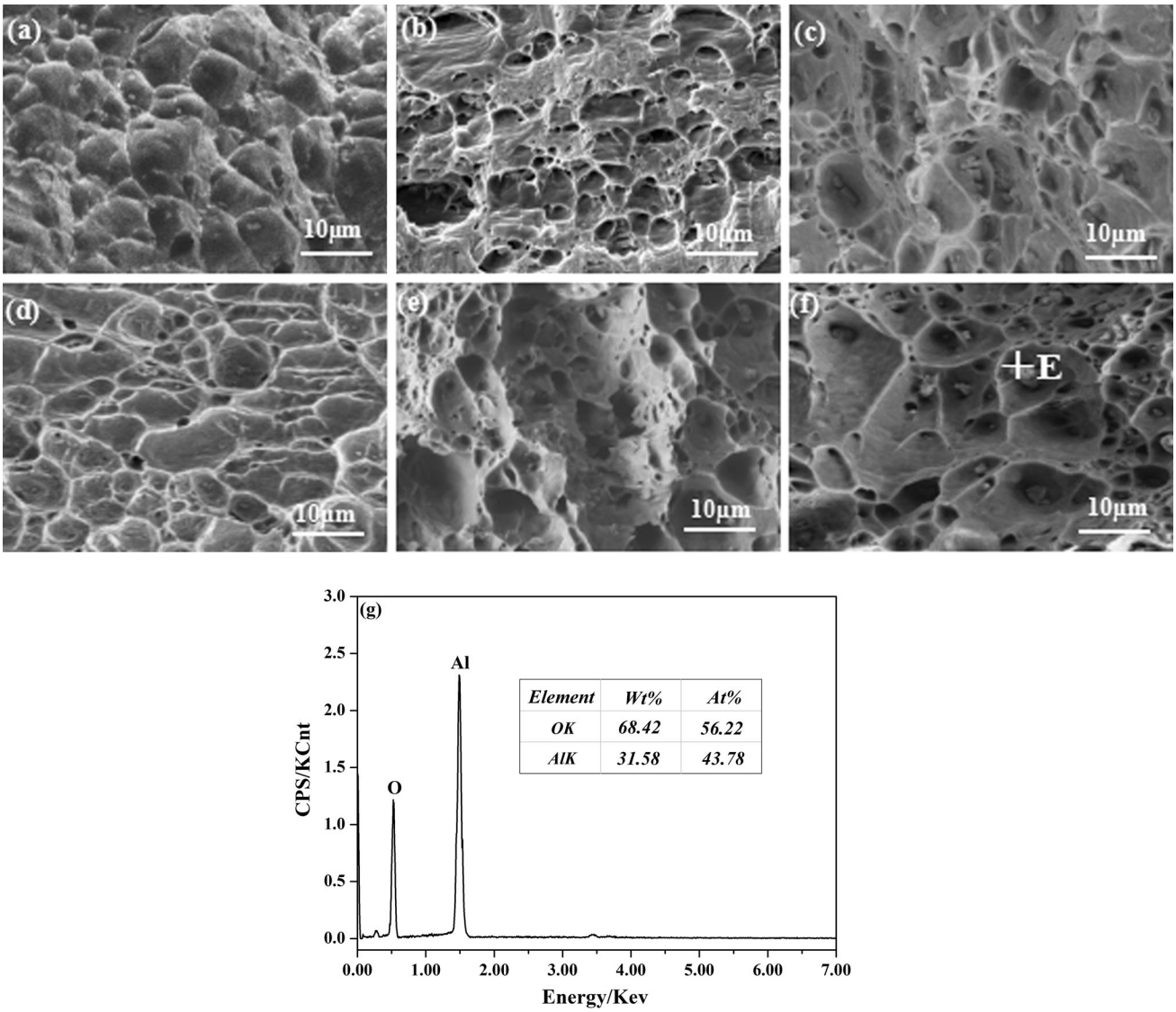

Fig. 11. Evolution of fracture morphology of SAC0307-0.12Al_2O_3/Cu solder joint subjected to thermal cycling: (a) 200 cycles; (b) 400 cycles; (c) 600 cycles; (d) 800 cycles; (e) 1000 cycles; (f) 1200 cycles; (g) EDS analysis of point E in (f).

0.3Ag-0.7Cu (SAC0307) and SAC0307-0.12Al_2O_3 nanoparticles (NPs) subjected to thermal cycling were investigated and the following conclusions can be obtained:

1. Adding Al_2O_3 NPs (0.12 wt%) can effectively inhibit the microstructure coarsening of the solder matrix subjected to thermal cycling due to the pinning effects of surface-active Al_2O_3 NPs on the IMCs' growth.
2. With increasing the number of thermal cycles, the thickness of both interfacial IMC layers (Cu_6Sn_5 + Cu_3Sn) increased. Theoretical analysis showed doping 0.12 wt% Al_2O_3 NPs effectively reduced the average growth coefficients of both total interfacial IMCs ($\bar{D}_T$) and Cu_3Sn IMCs ($\bar{D}_{Cu_3}$), from 9.2×10^{-11} cm^2/h to 5.6×10^{-11} cm^2/h, and from 6.9×10^{-11} cm^2/h to 4.1×10^{-11} cm^2/h, respectively.
3. Irrespective of the number of thermal cycles, the SAC0307-0.12Al_2O_3/Cu solder joint had a higher shear force than the SAC0307/Cu solder joint due to the improved joint microstructure caused by the doping of Al_2O_3 NPs, including the refinement of the solder matrix as well as the thinning and flattening of the interfacial IMC layer.
4. With the number of thermal cycles increased from 200 to 1200, the SAC0307-0.12Al_2O_3/Cu solder joint always displayed a typical ductile fracture mode, while the fracture mode for the SAC0307/Cu solder joint was transformed from ductile to a mixture of ductile and brittle. This

indicated a higher ductility of SAC0307-$0.12Al_2O_3$ than of SAC0307.

ACKNOWLEDGMENTS

This project is supported by National Natural Science Foundation of China (Grant No. 51675269) and the Priority Academic Program Development of Jiangsu Higher Education Institutions (PAPD).

REFERENCES

1. J. Wang, H. Wei, P. He, T.S. Lin, and F.J. Lu, *J. Electron. Mater.* 44, 3872 (2015).
2. G. Zeng, S.B. Xue, L.L. Gao, L. Zhang, Y.H. Hu, and Z.M. Lai, *J. Alloys Compd.* 509, 7152 (2011).
3. J. Gu, Y.P. Lei, J. Lin, H.G. Fu, and Z.W. Wu, *J. Electron. Mater.* 46, 1396 (2017).
4. D.A. Shnawah, M.F.M. Sabri, I.A. Badruddin, and F.X. Che, *J. Electron. Mater.* 41, 2631 (2012).
5. T. Kangasvieri, O. Nousiainen, J. Putaala, R. Rautioahob, and J. Vähäkangas, *Microelectron. Reliab.* 46, 1335 (2006).
6. M.A.A. Mohd Salleh, S. Mcdonald, and K. Nagita, *Appl. Mech. Mater.* 421, 260 (2013).
7. J. Wu, S.B. Xue, J.W. Wang, and M.F. Wu, *J. Alloys Compds* 784, 471 (2019).
8. G. Zeng, S.B. Xue, L. Zhang, W. Dai, and J.D. Luo, *J. Mater. Sci. Mater. Electron.* 21, 421 (2010).
9. L. Zhang, L. Sun, Y.H. Guo, and C.W. He, *J. Mater. Sci. Mater. Electron.* 25, 1209 (2014).
10. F. Gao, T. Takemoto, and H. Nishikawa, *Mater. Sci. Eng. A* 39, 420 (2006).
11. M.O. Alam, Y.C. Chan, and K.N. Tu, *Chem. Mater.* 15, 4340 (2003).
12. F. Wang, X. Ma, and Y. Qian, *Scr. Mater.* 53, 699 (2005).
13. C.Y. Lee, J.W. Yoon, Y.J. Kim, and S.B. Jung, *Microelectron. Eng.* 82, 561 (2005).
14. Y. Tian, C. Wang, X.S. Ge, P. Liu, and D.M. Liu, *Mater. Sci. Eng. B* 95, 254 (2002).
15. H. Lee, C. Kim, C. Heo, J.H. Lee, and Y.D. Kim, *Microelectron. Reliab.* 87, 75 (2018).
16. J. Mittal, S.M. Kuo, Y.W. Lin, and K.L. Lin, *J. Electron. Mater.* 38, 2436 (2009).
17. Q.B. Tao, L. Benabou, V.N. Le, H. Hwang, and D.B. Luu, *J. Alloys Compd.* 694, 892 (2017).
18. C.M.L. Wu, D.Q. Yu, C.M.T. Law, and L. Wang, *Mater. Sci. Eng. R Rep.* 44, 1 (2004).
19. L. Zhang, S.B. Xue, L.L. Gao, G. Zeng, Z. Sheng, Y. Chen, and S.L. Yu, *J. Mater. Sci. Mater. Electron.* 20, 685 (2009).
20. D.X. Luo, S.B. Xue, and Z.Q. Li, *J. Mater. Sci. Mater. Electron.* 25, 3566 (2014).
21. W.Q. Xing, X.Y. Yu, H. Li, L. Ma, W. Zuo, P. Dong, W.X. Wang, and M. Ding, *Mater. Sci. Eng. A* 678, 252 (2016).
22. K. Mehrabi, F. Khodabakhshi, E. Zareh, A. Shahbazkhan, and A. Simchi, *J. Alloys Compd.* 688, 143 (2016).
23. L. Zhang and K.N. Tu, *Mater. Sci. Eng. R* 82, 1 (2014).
24. C.X. Hou, Y. Hou, Y.Q. Fan, Y.J. Zhai, Y. Wang, Z.Y. Sun, R.H. Fan, F. Dang, and J. Wang, *J. Mater. Chem. A* 6, 6967 (2018).
25. N.N. Wu, C. Liu, D.M. Xu, J.R. Liu, W. Liu, Q. Shao, and Z.H. Guo, *ACS Sustain. Chem. Eng.* 6, 12471 (2018).
26. C.X. Hou, Z.X. Tai, L.L. Zhao, Y.J. Zhai, Y. Hou, Y.Q. Fan, F. Dang, J. Wang, and H.K. Liu, *J. Mater. Chem. A* 6, 9723 (2018).
27. N.N. Wu, D.M. Xu, Z. Wang, F.L. Wang, J.R. Liu, W. Liu, Q. Shao, H. Liu, Q. Gao, and Z.H. Guo, *Carbon* 145, 433 (2019).
28. L. Sun, M.H. Chen, C.C. Wei, L. Zhang, and F. Yang, *J. Mater. Sci. Mater. Electron.* 21, 1 (2018).
29. J. Shen and Y.C. Chan, *J. Alloys Compd.* 477, 552 (2009).
30. S. Cheng, C.M. Huang, and M. Pecht, *Microelectron. Reliab.* 75, 77 (2017).
31. S.K. Kang, D.Y. Shih, N. Donald, W. Henderson, T. Gosselin, A. Sarkhel, N.Y.C. Goldsmith, K.J. Puttlitz, and W.K. Choi, *JOM* 55, 61 (2003).
32. A.E. Hammad, *Mater. Des.* 52, 663 (2013).
33. J. Wu, S.B. Xue, J.W. Wang, J.X. Wang, and S. Liu, *J. Mater. Sci. Mater. Electron.* 28, 10230 (2017).
34. J. Wu, S.B. Xue, J.W. Wang, M.F. Wu, and J.H. Wang, *J. Mater. Sci. Mater. Electron.* 29, 7372 (2018).
35. H.T. Chen, B. Jiang, and N. Lu, *ISA Trans.* 79, 127 (2018).
36. H.T. Chen, B. Jiang, N. Lu, and W. Chen, *Neurocomputing* 306, 119 (2018).
37. X. Deng, R.S. Sidhu, P. Johnson, and N. Chawla, *Metall. Mater. Trans. A* 36, 55 (2005).